bioRxiv preprint doi: https://doi.org/10.1101/2023.05.10.540107; this version posted May 10, 2023. The copyright holder for this preprint (which was not certified by peer review) is the author/funder. All rights reserved. No reuse allowed without permission.

Molecular motor tug-of-war regulates elongasome cell wall synthesis dynamics in *Bacillus subtilis*

Stuart Middlemiss[1*], David M Roberts[2,1], James Grimshaw[1], Joshua M Edwards [2,1], Zikai Sun[3], Kevin D Whitley[1], Thierry Blu[3], Henrik Strahl[1], and Séamus Holden[2,1*]

1: Centre for Bacterial Cell Biology, Biosciences Institute, Faculty of Medical Sciences, Newcastle University, Newcastle upon Tyne, UK;

2: School of Life Sciences, University of Warwick, Gibbet Hill Campus, Coventry, UK.

3: Department of Electronic Engineering, The Chinese University of Hong Kong, Hong Kong.

*: Corresponding authors: seamus.holden@warwick.ac.uk, stuart.middlemiss@newcastle.ac.uk

ABSTRACT

Most rod-shaped bacteria elongate by inserting new cell wall material into the inner surface of the cell sidewall. This is primarily performed by a highly conserved protein complex, the elongasome, which moves processively around the cell circumference and inserts long glycan strands that act as barrel-hoop-like reinforcing structures, thereby giving rise to a rod-shaped cell. However, it remains unclear how elongasome synthesis dynamics and termination events are regulated to determine the length of these critical cell-reinforcing structures. To address this, we developed a method to track individual elongasome complexes around the entire circumference of *Bacillus subtilis* cells for minutes-long periods using single molecule fluorescence microscopy. We found that the *B. subtilis* elongasome is highly processive and that processive synthesis events are frequent terminated by rapid reversal or extended pauses. We found that cellular levels of RodA regulate elongasome processivity, reversal and pausing. Our single molecule data, together with stochastic simulations, show that elongasome dynamics and processivity are regulated by molecular motor tug-of-war competition between several, likely two, oppositely oriented peptidoglycan synthesis complexes bound to the MreB filament. Our data, thus, demonstrate that molecular motor tug-of-war is a key regulator of elongasome dynamics in *B. subtilis*, which likely also regulates the cell shape via modulation of elongasome processivity.

bioRxiv preprint doi: https://doi.org/10.1101/2023.05.10.540107; this version posted May 10, 2023. The copyright holder for this preprint (which was not certified by peer review) is the author/funder. All rights reserved. No reuse allowed without permission.

INTRODUCTION

Almost all bacteria are encased by a peptidoglycan-based cell wall, which is essential for their survival. To maintain a robust cell wall during growth and division, bacterial cell wall synthesis proteins must accurately and reliably expand and remodel a precisely shaped structure more than 100 times their size. Due to the high internal turgor of a bacterial cell, major errors in cell wall synthesis lead to lethal cell lysis. For this reason, the cell wall synthesis machinery is the principal target of many first-line antibiotics such as β-lactams, as well as last resort antibiotics such as vancomycin and daptomycin that are used to treat infections caused by multidrug resistant pathogens. A better understanding of the biophysical principles of cell wall synthesis is therefore critical for deciphering how this highly successful class of antibiotics can induce bacterial cell death, for developing the next generation of cell-wall-targeting antibiotics, as well as developing countermeasures against the adaptive processes bacteria utilise to evade those already in clinical use.

Most rod-shaped bacteria, including key model organisms such as Gram-positive *B. subtilis* and Gram-negative *Escherichia. coli*, elongate by inserting new cell wall material into the inner surface of the cell wall. This is primarily performed by a highly conserved protein complex, the elongasome, which inserts long peptidoglycan strands circumferentially around the cell, giving rise to a rod-shaped cell morphology [1,2].

Gram-positive rod-shaped bacteria such as *B. subtilis* have a single cytoplasmic membrane surrounded by a thick multi-layered peptidoglycan cell wall. Elongasome-driven cell wall synthesis is performed pairs of enzymes comprised of the glycosyltransferase RodA, which polymerizes glycan strands; and a cognate class B transpeptidase (PBP2A or PBPH in *B. subtilis*) which attaches new strands to the existing cell wall [3]. These proteins, together with additional regulatory factors, are associated with the actin-homolog MreB, which forms antiparallel oriented ~200 nm long double-filament structures [4]. These cytoskeletal structures guide peptidoglycan insertion perpendicular to the long axis of the cell [5]. *B. subtilis* also encodes two functionally redundant MreB homologues, Mbl and MreBH, which copolymerize with MreB [6]. As continuous glycan chains can stretch less than cross-linked peptides, circumferentially oriented glycan strands reinforce the cell sidewall and thereby establish a rod-like cell shape [1,2]. The overall level of elongasome-driven cell wall synthesis plays a major role in establishing both the all overall rod shape morphology and the specific cell diameter; high levels of elongasome-driven cell wall synthesis lead to stiff, narrow, rod-shaped cells whereas low levels lead to soft, wide, spherical cells [1,2].

The processive motion of the elongasome is driven by peptidoglycan synthesis [7–9]. It is likely that the initial length of elongasome-synthesized glycan strands is determined by the processivity of the elongasome, i.e., the distance that elongasomes move during an individual processive synthesis event. As the primary function of the elongasome is to maintain rod-shape and elongate the cell sidewall by inserting circumferential glycan strands, we hypothesized that elongasome processivity, and thus the length of elongasome-synthesized glycan strands, is likely to have substantial effect on cell wall stiffness and thereby cell shape. Put simply – if elongasome synthesized glycans act as reinforcing structures similar to metal hoops around a wooden barrel, the length of those reinforcing structures should determine the stiffness of the cell's short axis.

To test these hypotheses, we developed a new method to track individual elongasome complexes around the entire cell circumference for minutes-long periods. We found that the *B. subtilis* elongasome is highly processive and exhibits frequent reverses and pauses. Intriguingly, we found that cellular levels of RodA regulate elongasome processivity, reversal and pausing. Together with stochastic simulations, our single molecule data support an end-binding tug-of-war model where competition between two opposing peptidoglycan synthesis complexes, bound to each end of the

bioRxiv preprint doi: https://doi.org/10.1101/2023.05.10.540107; this version posted May 10, 2023. The copyright holder for this preprint (which was not certified by peer review) is the author/funder. All rights reserved. No reuse allowed without permission.

symmetrical MreB double filament, determine elongasome dynamics and processivity. Elongasome tug-of-war may also regulate *B. subtilis* cell shape via modulation of elongasome processivity. Our data demonstrate that molecular motor tug-of-war is a key regulator of elongasome dynamics, which may also play a major role in bacterial cell shape control in *B. subtilis.*

RESULTS

The *B. subtilis* elongasome is highly processive and frequently reverses and pauses

Previously, it was only possible to track elongasomes that are performing cell wall synthesis over distances less than about 500 nm, owing to the geometrical limitations of total internal reflection fluorescence (TIRF) imaging, which is usually used for such measurements but only illuminates a small fraction of the cell circumference [18, 19]. Previous estimates of elongasome processivity have been in the range of 400-600 nm [10], suggesting that these measurements were limited by the shallow illumination depth of the technique.

To address this limitation, we combined single molecule tracking with VerCINI (vertical cell imaging by nanostructured immobilization), a method we developed to orient rod-shaped cells perpendicular to the microscope imaging plane [11]. We used single molecule VerCINI (smVerCINI) to focus on a slice of the bacterial cell sidewall approximately 0.5 µm thick (determined by the microscope objective depth of field), and tracked individual membrane bound MreB molecules in live *B. subtilis* cells using a previously characterized functional, native-locus MreB-HaloTag fusion [5]. We used a sub-stoichiometric labelling concentration of the bright cell-permeable JF549 (HaloTag ligand) JaneliaFluor dye [12] to sparsely label individual MreB molecules within membrane-bound MreB filaments (Fig. 1a). Because MreB motion is circumferential [5,13], MreB filament dynamics are mostly constrained to within the VerCINI focal plane, allowing long term imaging of MreB filament dynamics (Fig. 1a).

We tracked MreB molecules using long (500 ms) camera exposure times such that freely diffusive molecules were not detected, allowing us to exclusively analyse MreB molecules assembled within membrane bound MreB filaments, while simultaneously reducing effective photobleaching rate using long (6 s) strobe intervals. We found that MreB filaments remain assembled at the membrane for extended periods of time, frequently reverse direction and sometimes pause for extended periods (Fig. 1b-c). As MreB filament motion is dependent on peptidoglycan synthesis, motile MreB filaments should correspond to fully assembled elongasome complexes actively engaged in peptidoglycan synthesis. Paused MreB filaments could correspond either to filaments where some or all the other critical elongasome components are missing/ unbound, or to fully assembled complexes, which are not currently synthesizing peptidoglycan.

We determined the binding lifetime of MreB subunits within filaments by stroboscopic illumination to be 128 s [95% CI: 109, 164] (Fig. 1d-e, [14]), showing that the MreB filaments remain assembled at the membrane for extended periods of time. This measurement represents a lower bound on the lifetime of both assembled MreB filaments, as it will be limited by occasional migration of the elongasome complexes beyond the microscope depth of field, and possibly by slow dissociation of MreB subunits from the MreB filament.

bioRxiv preprint doi: https://doi.org/10.1101/2023.05.10.540107; this version posted May 10, 2023. The copyright holder for this preprint (which was not certified by peer review) is the author/funder. All rights reserved. No reuse allowed without permission.

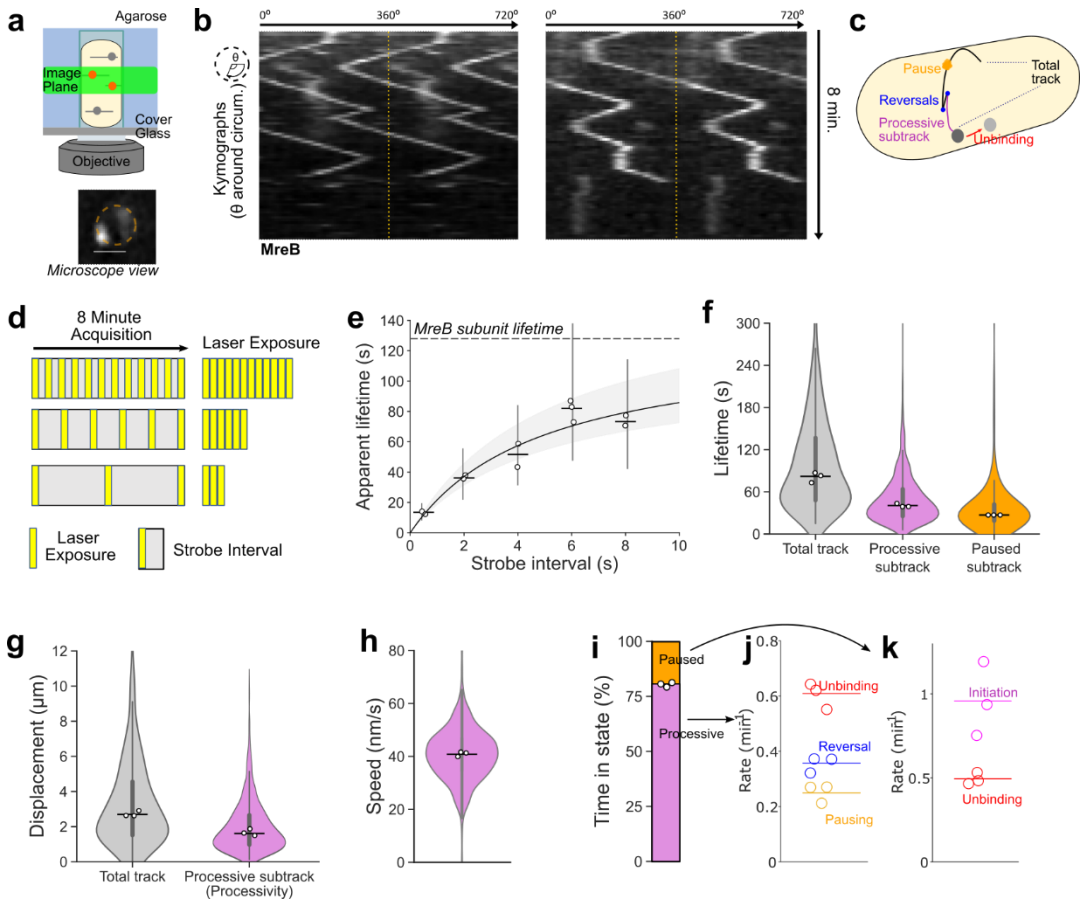

Figure 1: Single molecule VerCINI (smVerCINI) measurements of MreB dynamics. (a) Principle of smVerCINI. Grey lines represent individual MreB filaments, orange circles indicate MreB subunits sparsely labelled with JF549 fluorophore. **(b)** Exemplar kymographs of MreB filament dynamics. Kymographs are measured around the cell circumference. Two full revolutions around the cell (0–720°) are plotted side-by-side to resolve filament trajectories that pass 0°/360°, separated by yellow dotted lines. **(c)** Cartoon illustrating different types of MreB filament dynamics observed. **(d)** Principle of stroboscopic illumination: increasing intervals between constant illumination time reduce photobleaching and allow estimation of photobleaching rate and molecule unbinding rate. **(e)** Stroboscopic illumination plot of strobe interval versus apparent MreB subunit lifetime. Black line: non-linear fit of Gebhardt model (Methods). Grey area: 95% CI on fitted model. Horizontal dashed line: estimated MreB subunit lifetime. Vertical lines: IQR of apparent lifetimes. Fitted subunit lifetime τ_{off}=128 s [95% CI: 109, 164], photobleaching lifetime, τ_{off}=13s [95% CI: 11, 16]. **(f-g)** MreB filament lifetime and circumferential track displacement for individual tracks and processive or static subtracks. **(h)** MreB filament speed for processive subtracks. **(i)** Time MreB filaments spend in each motion state. **(j-k)** Single molecule switching rates for MreB processive subtracks *(j)* and static subtracks *(k)*. Measurements in *b, f-k* performed at 6 s strobe interval. White filled circles: median of biological replicates. Horizontal lines: median of all data points. Violin plots: Thick error bar lines indicate IQR, thin lines indicate adjacent vales. Strain used: *B. subtilis* SM01 (*mreB-HaloTag, Δhag*).

We next characterized MreB motility by smVerCINI. We chose a strobe interval of 6 s, which extended the effective photobleaching lifetime 12-fold to 156 s [95% CI: 132, 192] (Fig. 1e), longer than the median observed MreB subunit lifetime. This allowed direct measurements of MreB single molecule switching kinetics. We found that MreB filaments are motile 81 % of the time, [Range: 79-81, *n=3*], and immobile (paused) the rest of the time (Fig. 1i). MreB filaments frequently switch between motile and paused states, and motile molecules frequently change direction (reversal) (Fig. 1i-k). The median lifetimes of both the processive and paused motility states were substantial: 40.5 s [95% CI: 39.0, 43.0] and 27.0 s [95% CI: 24.0, 29.5], respectively.

bioRxiv preprint doi: https://doi.org/10.1101/2023.05.10.540107; this version posted May 10, 2023. The copyright holder for this preprint (which was not certified by peer review) is the author/funder. All rights reserved. No reuse allowed without permission.

While elongasome pauses and reversals have been observed before, they were previously thought to be rare events [10,15], likely due to elongasome trajectory truncation due to TIRF imaging. Strikingly however, we found that 51 % [Range: 48-52, *n=3*] of elongasome processive synthesis events are terminated by changes in elongasome dynamics - reversal or pausing – rather than by elongasome disassembly or MreB dissociation (Fig. 1j). These data thus demonstrate that bidirectional elongasome motility is a central feature of elongasome dynamics. Furthermore, given that so many synthesis events terminate due to changes in motility state rather than disassembly/ dissociation, elongasome bidirectional motility must play a significant role in determining elongasome processivity.

Using smVerCINI, we found that MreB filaments, and therefore *B. subtilis* elongasomes, are highly processive. Complete MreB tracks were found to contain multiple substrates, where MreB was observed either to move processively in the same direction at constant speed – corresponding to active cell wall synthesis [7–9], or to pause for extended periods. Processive subtracks were found to have a median displacement of 1.61 µm [95% CI: 1.51, 1.69] (Fig.1g), or approximately 180° around the cell circumference. This is substantially greater than the 0.5 µm previously estimated by TIRF [10]. We found that MreB moved at constant speed, independent of the processive subtrack lifetime (Fig. 1h, SI Fig. 2b). As this processivity likely determines the initial length of elongasome-synthesized glycan strands, these data support a model where the elongasome-synthesized peptidoglycan strands acts as major reinforcing structural elements in the cell sidewall, much like hoops around a barrel.

Given that cell wall synthesis rates correlate with cell growth, we wondered how cell growth rate affected elongasome processivity. Surprisingly, we found that large 3-fold changes in growth rate have only a modest effect on elongasome processivity and switching dynamics (Supplementary Figure 3). Deletion of *mltG*, which has been proposed as a possible terminator of peptidoglycan synthesis [16] also showed minimal effect on elongasome processivity (Supplementary Figure 4).

bioRxiv preprint doi: https://doi.org/10.1101/2023.05.10.540107; this version posted May 10, 2023. The copyright holder for this preprint (which was not certified by peer review) is the author/funder. All rights reserved. No reuse allowed without permission.

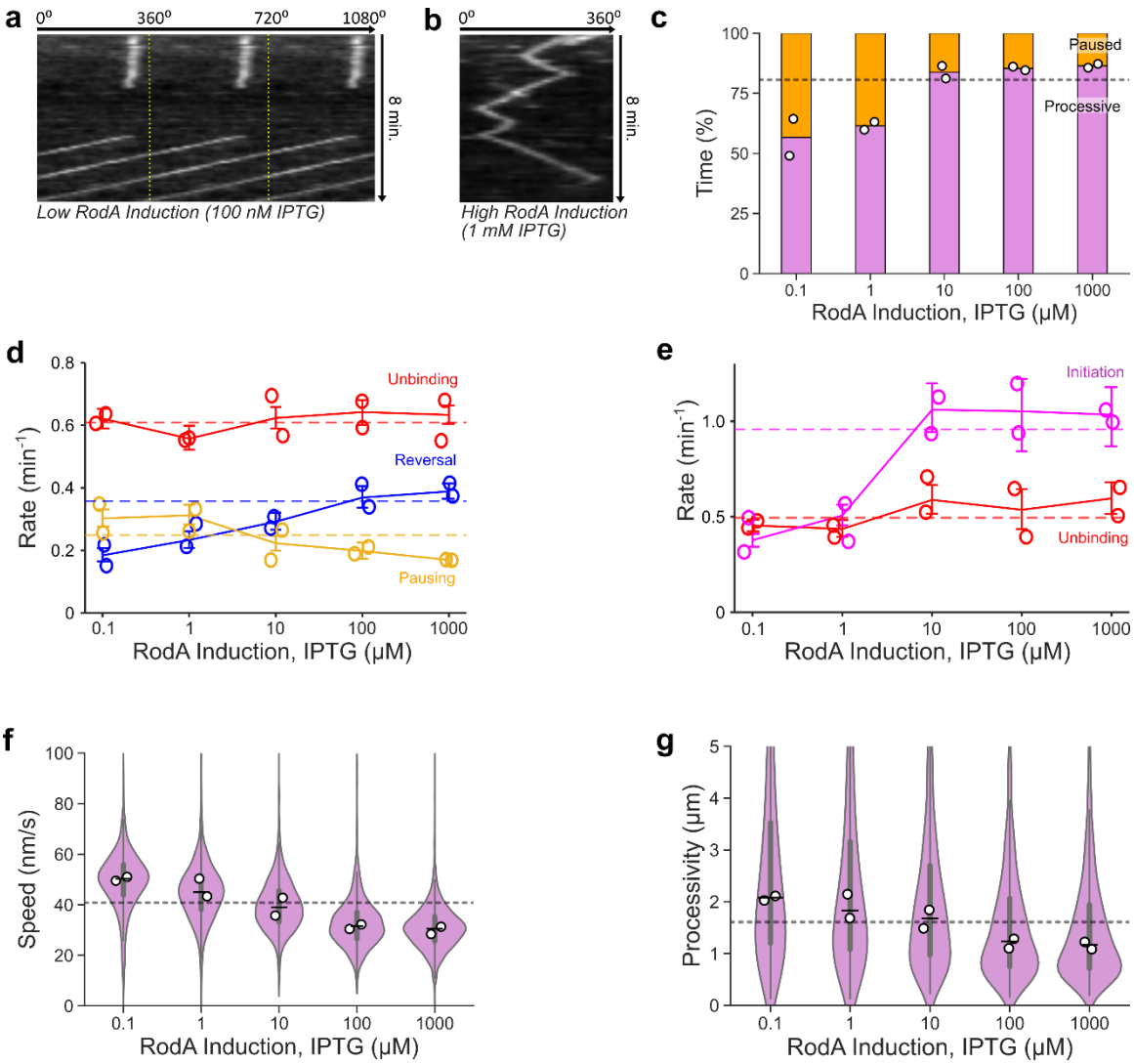

Figure 2: Effect of cellular levels of RodA on MreB dynamics. (a-b) Exemplar kymographs of MreB filament dynamics at low *(a)* and high *(b)* RodA levels achieved through expression from an IPTG-inducible promoter. Kymographs are measured around the cell circumference. More examples are shown in Supplementary Figure 9. **(c)** Time MreB filaments spend in each motion state as a function of *rodA* expression level. **(d-e)** Single molecule switching rates for MreB processive subtracks (d) and static subtracks (e). Solid coloured lines represent medians of all data points for each condition. **(f-g)** MreB filament speed and processivity for processive subtracks. White filled circles: median of biological replicates. Horizontal dashed lines: value of each parameter (eg rate, speed) at native *rodA* expression level in strain SM01 (*mreB-HaloTag, Δhag*). Narrow horizontal lines: median of all data points. Violin plots: thick error bar lines indicate IQR, thin lines indicate adjacent values. Strain used: *B. subtilis* SM28 (*mreB-HaloTag*, *Pspac-rodA, Δhag*). Further quantification in Supplementary Figure 7.

RodA expression level regulates bidirectional motility and elongasome processivity

It was previously speculated that elongasome reversals could be caused by molecular motor tug-of-war, whereby two or more RodA-PBP2A/ PBPH synthesis complexes attached to a symmetrical MreB-filament pull in opposite directions [18], similar to eukaryotic organelle transport [17]. However, this proposal was not widely accepted as bidirectional motility of elongasomes was until now assumed to be a rare, inconsequential feature of elongasome dynamics, as well as due to other limitations in the original tug-of-war model, outlined in the next section.

Given our frequent observation of elongasome reversals and pauses which are strongly reminiscent of eukaryotic molecular motor tug-of-war, we set out to test whether elongasome complexes might

bioRxiv preprint doi: https://doi.org/10.1101/2023.05.10.540107; this version posted May 10, 2023. The copyright holder for this preprint (which was not certified by peer review) is the author/funder. All rights reserved. No reuse allowed without permission.

indeed participate in molecular motor tug-of-war, and to determine whether tug-of-war mediated reversals might thereby determine elongasome processivity.

We titrated cellular levels of the elongasome transglycosylase, RodA, in a strain with inducible expression from the native locus (*rodA::*P_{spac}*-rodA* [2]), and measured elongasome dynamics by smVerCINI of MreB-HaloTag. At low *rodA* expression levels, we observed that elongasomes exhibited extended pauses, infrequent reversals, and high speed (Fig. 2, Supplementary Figure 9). In contrast, at high *rodA* expression, pauses were rare, reversals more frequent and speeds lower (Fig. 2d). MreB pausing rate decreased 0.43-fold (-0.13 min^{-1} difference [95% CI: -0.17,-0.10]), reversal rate increased 1.1-fold (0.20 min^{-1} difference [95% CI: 0.17,0.24]) and motile MreB speed decreased 0.39-fold (-19.7 nm s^{-1} difference [95% CI:-20.3 ,-19.3]) at high vs low *rodA* expression levels (1mM IPTG vs 100 nM IPTG induction, Figure 2d,f). No change was detected in MreB unbinding rate (0.01 min^{-1} difference [95% CI: -0.03,0.06] (Fig. 2d), consistent with MreB movement being driven by peptidoglycan synthesis rather than MreB polymerisation/depolymerisation. Intriguingly, MreB processivity decreased 0.44-fold, (-0.91 µm difference [95% CI: -1.02, -0.78]) between high and low *rodA* expression, and the processivity of cells expressing *rodA* from the native promotor was near the mid-point of this range (Fig. 2g).

Together, these data show that elongasome dynamics and processivity are sensitively regulated by the cellular concentration of RodA. The data are consistent with a model where increased RodA levels lead to more active synthesis complexes bound to each MreB filament, thereby causing more frequent incidences of tug-of-war between oppositely oriented synthesis complexes, leading to frequent rapid elongasome reversals. These data are also consistent with a model where high levels of tug-of-war reduce the overall elongasome processivity as a result of more frequent reversals and reduced average elongasome speed due to drag from competing synthesis complexes.

One possible alternative model is that elongasome reversals could be caused by collisions between two elongasome complexes. TIRF-structured illumination microscopy (SIM) has previously been used to observe isolated MreB filaments undergoing reversals without any other filaments nearby to collide with, inconsistent with the collision model [7,18]. In a third model, elongasome reversals could be caused by interactions with existing peptidoglycan; if, for example, glycans oriented at certain angles could act as effective barriers to the elongasome. While it is possible that interactions with the peptidoglycan may play some role in elongasome bidirectional motility, that model does not explain why elongasome reversal rate increases, or why pausing rate decreases, as *rodA* expression level is increased.

We also tested how single knockouts of the redundant elongasome transpeptidases PBP2A (*pbpA*) and PBPH (*pbpH*) affected elongasome dynamics. Deletions of these genes had little effect elongasome switching kinetics, speed or processivity (Supplementary Figure 4). These results support a model where the elongasome transpeptidases are in excess compared to RodA, and that RodA concentration, or its assembly to an elongasome complex, is the principal factor controlling the concentration of active elongasome synthesis complexes within the cell any given time.

bioRxiv preprint doi: https://doi.org/10.1101/2023.05.10.540107; this version posted May 10, 2023. The copyright holder for this preprint (which was not certified by peer review) is the author/funder. All rights reserved. No reuse allowed without permission.

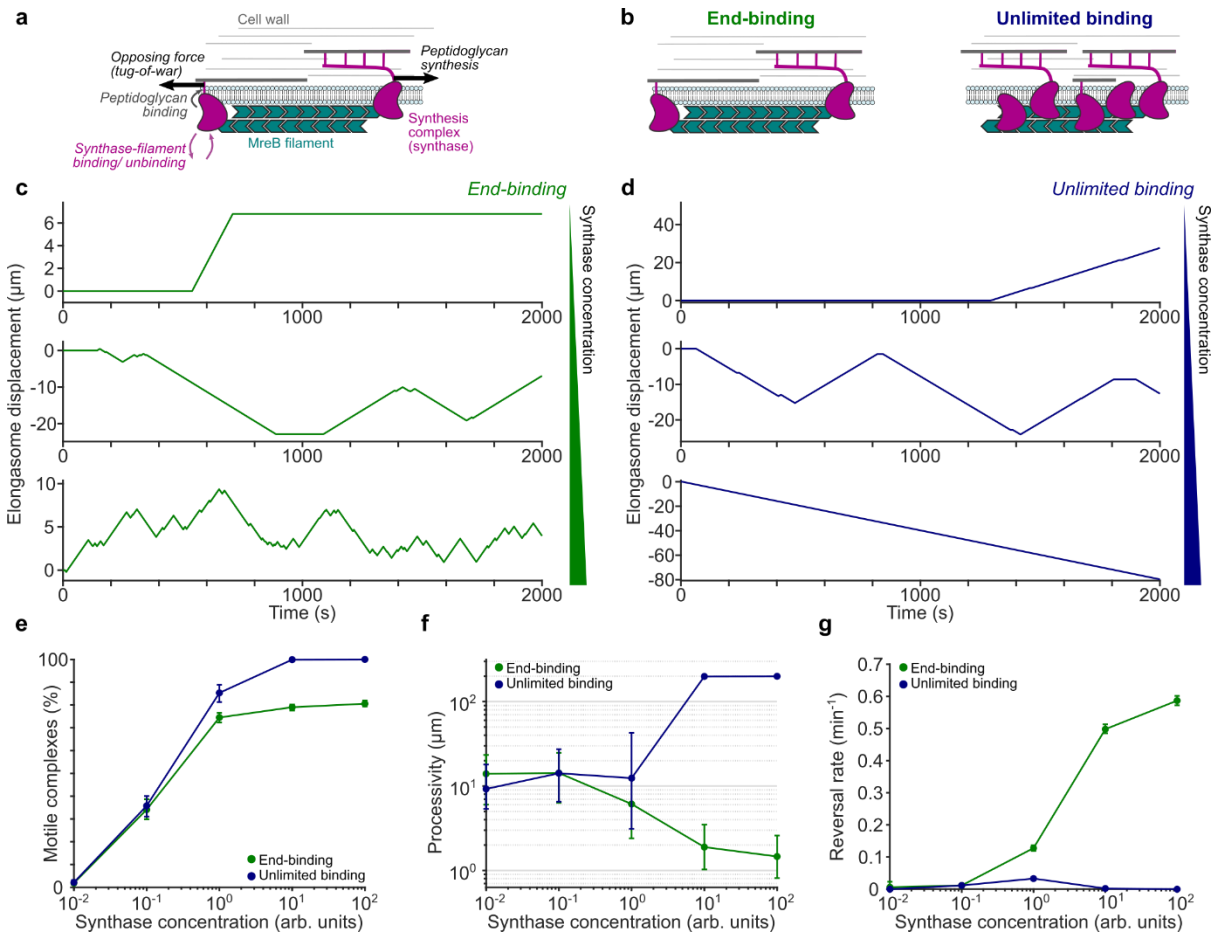

Figure 3: Simulations of elongasome tug-of-war dynamics. (a) Cartoon of elongasome complex dynamics as implemented in the stochastic model. **(b)** Illustration of the two models of elongasome tug-of-war tested: *end-binding*, where only one synthesis complex can bind to each end of the antiparallel MreB double filament, in opposite directions; *unlimited binding*, where multiple synthesis complexes can bind along the MreB filament. **(c-d)** Examples of simulated elongasome dynamics at low (10^{-2} arb. Units), intermediate (10^{0} arb. Units) and high (10^{2} arb. Units) synthesis complex (synthase) concentrations for end-binding and unlimited binding models. **(e-g)** Fraction of motile elongasomes, processivity and reversal rate as a function of synthesis complex concentration for both models. Solid coloured lines with filled circles, sample medians; vertical lines, 95% CI.

Stochastic simulations show that an end-binding tug-of-war model can explain experimentally observed effects of RodA expression level on elongasome processivity and bidirectional motility

Previously, it was proposed that elongasome tug-of-war between many synthases bound along the entire MreB filament might regulate elongasome dynamics [18]; a scenario which we term the *unlimited binding* elongasome tug-of-war model (Fig. 3b). However, this model was not widely accepted as the bidirectional motility of elongasomes was until now assumed to be a relatively unimportant feature of elongasome dynamics, mostly due to underestimation of elongasome pausing and reversal rates [10,15]. The *unlimited-binding* tug-of-war model also assumed large numbers of competing synthesis complexes bound to a single MreB filament, which has since been found to be unlikely [13] and predicted a strong dependence of elongasome speed upon MreB filament speed which was later found not to be the case [13]. Furthermore, previous theoretical work on eukaryotic molecular motors showed that as more molecular motors are added to an *unlimited-binding* tug-of-war scenario, a runaway scenario occurs where reversals become exponentially less likely as a single opposing motor must win the tug-of-war against an ever-greater number of engaged motors [19]. Taken together, the *unlimited-binding* model is not easy reconcile with our observations that MreB

bioRxiv preprint doi: https://doi.org/10.1101/2023.05.10.540107; this version posted May 10, 2023. The copyright holder for this preprint (which was not certified by peer review) is the author/funder. All rights reserved. No reuse allowed without permission.

reversal rate increases and processivity decreases at high RodA levels. To address this, and inspired by the observation that MreB forms a symmetric antiparallel double filament [4], we propose an *end-binding* elongasome tug-of-war model, where at most two synthesis complexes can bind to an MreB filament, one at each end, pointing in opposite directions (Fig. 3b). The *end-binding* model inherently avoids large numbers of synthesis complexes per filament, as well as the highly processive multi-motor scenario. Alternatively, we speculated that the *unlimited-binding* model might potentially be able to explain our experimental observations if cellular concentrations of elongasome synthesis complex components are low enough to limit the number of synthesis complexes per MreB filament to around 1-2 on average, and thereby mostly avoid the runaway elongasome scenario.

To test these two models, we used Monte Carlo simulations to evaluate whether either the *end-binding* or *unlimited-binding* synthase tug-of-war models are physically plausible mechanisms to regulate elongasome reversal rate and processivity. The simulations are an extension of the Müller, Klumpp, and Lipowsky (MKL) model of eukaryotic cargo transport [19], and assume that that multiple RodA-bPBP synthesis complexes can bind to both the MreB filament and the existing cell wall to initiate peptidoglycan synthesis (Fig. 3a, Supplementary Note 1). Synthesis complexes attempting to perform peptidoglycan synthesis in opposite directions will stall and briefly engage in tug-of-war, resulting in either resumption of peptidoglycan synthesis in the original direction, or reversal and initiation of peptidoglycan synthesis in the opposite direction.

We performed simulations of each model over a range of synthesis complex concentrations, using an extension of the MKL model to allow concentration dependent binding/ unbinding of synthesis complexes from the MreB filament (Fig. 3, Supplementary Figure 5, Supplementary Note 1). Both models showed extended elongasome pausing and infrequent reversals at low synthesis complex concentrations (Fig. 3), similar to experimental measurements (Fig. 2). At intermediate synthesis complex concentration, elongasome reversal rate increased for both the *end binding* and *unlimited binding* models. At high synthesis complex concentrations, the *end binding* model still showed frequent reversals, consistent with our experimental data. However, the reversal rate for the *unlimited binding model* declined rapidly once the average number of bound synthesis complexes increased beyond two (Fig 3G). We also found that as synthesis complex concentration increased, the *end binding* model processivity decreased in a manner consistent with our experimental observations. While the *unlimited binding* model shows a transient increase in reversal rate at intermediate synthase concentrations, which could potentially partially reproduce experimental results, even in this regime we were not able to reproduce the experimentally observed increase in processivity as a function of synthase concentration in simulations of the *unlimited binding* model as implemented here.

These data show that an *end-binding* synthase tug-of-war model is a physically plausible model that is sufficient to recapitulate experimentally observed trends in elongasome reversal rate and processivity. Interestingly, this model also makes strong predictions about the structure, location and number of RodA-bPBP complexes on MreB filaments, which could be tested in future to better understand the molecular mechanisms underlying elongasome tug-of-war.

Cell widening upon *rodA* overexpression may be driven by tug-of-war mediated reduction in elongasome processivity

RodA protein levels have previously been shown to control *B. subtilis* cell width in a non-trivial manner [2]: low or high RodA levels lead to abnormally wide cells, whereas intermediate levels ensure narrower, wild-type-like cell morphology. We confirmed that the cell widening phenotype upon *rodA* overexpression also occurred in the minimal media and culture conditions used in this study (Fig. 4a, Supplementary Figure 8a).

bioRxiv preprint doi: https://doi.org/10.1101/2023.05.10.540107; this version posted May 10, 2023. The copyright holder for this preprint (which was not certified by peer review) is the author/funder. All rights reserved. No reuse allowed without permission.

Recent studies support a model where that cellular levels of motile elongasomes determine cell width by controlling the density of newly synthesized circumferentially oriented glycan strands and thus regulating lateral cell wall stiffness. This model predicts that cell width decreases as elongasome synthase concentration increases [2]. However, this model is insufficient to explain the increase in cell width upon overexpression of *rodA* [2]. We found that cell widening upon *rodA* overexpression is not associated with any detectable change in surface density of motile MreB filaments (Fig. 4b), which have previously been shown to regulate cell width [2], nor any detectable change in cell growth rate (Supplementary Figure 8b).

Our findings that RodA levels determine elongasome processivity via tug-of-war mediated regulation (Fig. 2-3) provide a simple mechanistic model for the complex dependence of cell width on cellular RodA levels. We hypothesize that cells must maintain a balance between: (i) elongasome pausing at low synthase levels, which reduces cellular levels of motile elongasomes; and (ii) tug-of-war at high synthase levels, which reduces elongasome processivity (Fig. 2). Since elongasome synthesized glycan strands act to reinforce the cell sidewall, both the length and total number of elongasome synthesized glycans should determine cell sidewall stiffness and width. Therefore, an optimally stiff, narrow cell wall would be synthesized at intermediate synthase concentration levels, which balances the opposing constraints of density of active elongasomes and elongasome processivity (Fig. 5).

It was previously speculated that cell widening upon *rodA* overexpression could be caused by high levels of disorganized synthesis by RodA-bPBP complexes not bound to the elongasome [2]. However, experimental evidence has not yet been presented for that hypothesis. Further experiments will be required to conclusively determine whether elongasome tug-of-war, off-target RodA-bPBP synthesis or a combination of both drive cell widening upon *rodA* overexpression.

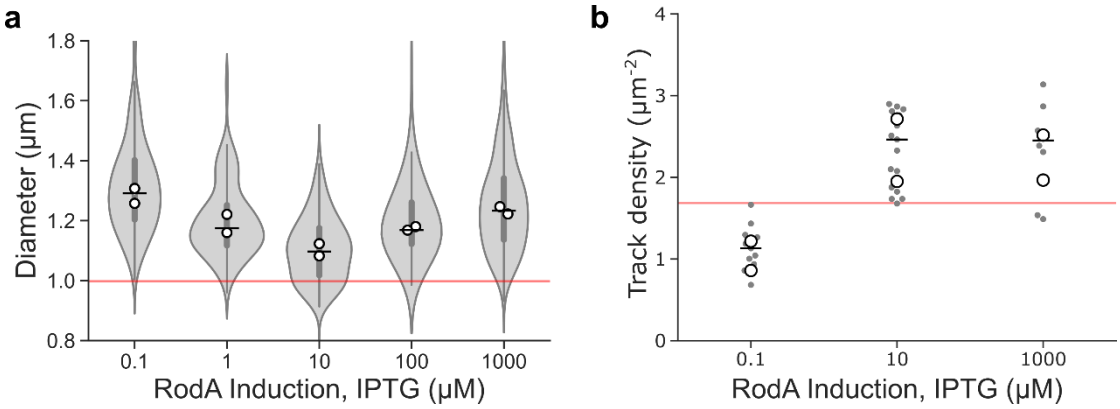

Figure 4: Effect of cellular levels of RodA on cell shape and MreB filament density. Effect of titration of RodA cellular levels expressed as sole cellular copy from an inducible promotor on **(a)** cell diameter, and **(b)** surface density of motile MreB filaments measured by SIM-TIRF microscopy. Horizontal lines show overall median. Vertical lines indicate IQR. White filled circles indicate biological replicates. Grey filled circles indicate medians of each field of view in SIM-TIRF experiments. Red line indicates values for native RodA levels. Strain used: *B. subtilis* SM28 (*mreB-HaloTag*, *Pspac-rodA, Δhag*).

bioRxiv preprint doi: https://doi.org/10.1101/2023.05.10.540107; this version posted May 10, 2023. The copyright holder for this preprint (which was not certified by peer review) is the author/funder. All rights reserved. No reuse allowed without permission.

DISCUSSION

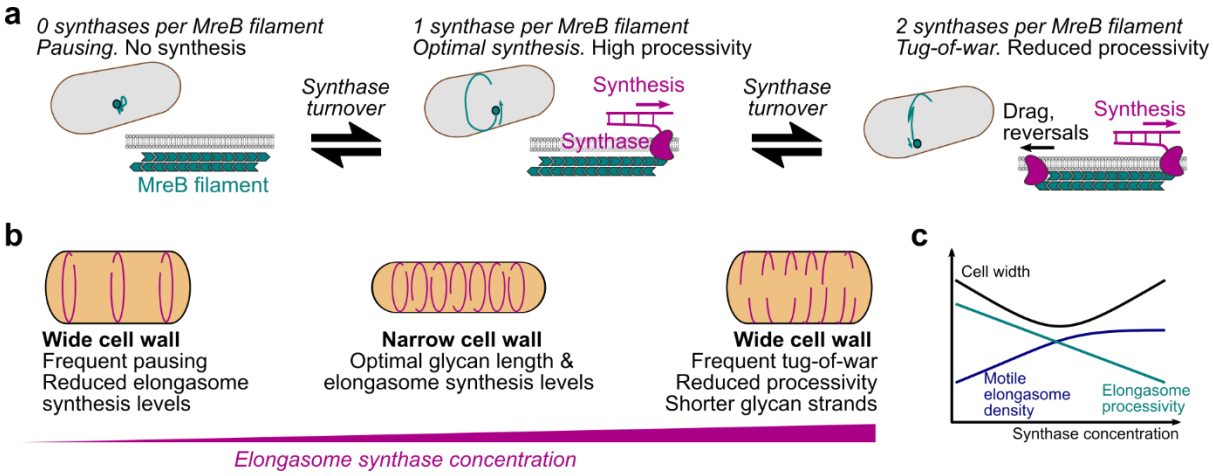

Figure 5: Tug-of-war model of elongasome dynamics and cell size regulation. (a) Model for effect of number of bound active synthesis complexes on elongasome dynamics. Note that synthases refer to complete synthesis complexes, i.e., active RodA-bPBP pairs. **(b-c)** Speculative model for effect of elongasome synthase concentration on cell shape.

The elongasome plays a central role in cell wall growth and maintenance of cell shape in a wide range of bacteria. In this study, we found that *B. subtilis* elongasomes are highly processive, with each event covering on average half the cell circumference, supporting a model where elongasome synthesized glycan strands function as major structural elements that reinforce the cell sidewall. We found that bidirectional motility – reversal and pausing – is not a rare curiosity as thought previously, but is a central feature of elongasome dynamics. We showed that elongasome processivity and bidirectional motility is regulated by molecular motor tug-of-war between multiple, likely maximally two, synthesis complexes bound in opposite directions on individual MreB filaments. We also found evidence that elongasome tug-of-war may regulate cell size and shape via modulation of elongasome processivity, and thereby the length of new glycan strands. These results establish molecular motor tug-of-war acts as a major regulator of bacterial cell wall synthesis activity.

Our study shows that molecular motor tug-of-war, previously thought to be a phenomenon exclusive to eukaryotic molecular motors, regulates MreB-cytoskeleton-associated cell wall synthesis in the model bacterium *B. subtilis*. Similar to bidirectional molecular motor transport in eukaryotes [17], molecular motor tug-of-war enables straightforward tuning of synthase dynamics, and could thereby facilitate rapid regulation of cell wall material properties, by regulating the concentration or activity of the Rod-complex. Tug-of-war mediated bidirectional motility may also allow obstacles in the cell wall to be avoided and peptidoglycan synthesis to be distributed evenly around the surface of the cell wall. Further studies will be required to determine the detailed molecular principles underlying elongasome tug-of-war and to conclusively determine the role and extent of molecular motor tug-of-war in regulating bacterial cell shape.

ACKNOWLEDGEMENTS

We thank Yoshi Kawai, Jeff Errington, Richard Daniel (Newcastle) and Ethan Garner (Harvard) for strains. We thank Cees Dekker (TU Delft, Netherlands) for nanofabricated VerCINI wafers and Luke Lavis (Janelia Farm, USA) for Janelia Fluor dyes. SH acknowledges funding support by a Wellcome Trust & Royal Society Sir Henry Dale Fellowship grant number 206670/Z/17/Z. SM and HS were supported

bioRxiv preprint doi: https://doi.org/10.1101/2023.05.10.540107; this version posted May 10, 2023. The copyright holder for this preprint (which was not certified by peer review) is the author/funder. All rights reserved. No reuse allowed without permission.

by UK Biotechnology and Biological Sciences Research Council (BBSRC) doctoral studentship (BB/M011186/1) and grant (BB/S00257X/1), respectively.

AUTHOR CONTRIBUTIONS

SM and JG created and characterised bacterial strains. SM, DMR and SH performed experiments. SM, DMR and SH analysed data. ZS and TB developed PureDenoiseGPU software. KW tested PureDenoiseGPU software. SH performed simulations. JE designed and built one of the custom microscopes used in the study. SH, SM and HS designed experiments. SH directed the research. SH and SM wrote the manuscript with input from all authors.

bioRxiv preprint doi: https://doi.org/10.1101/2023.05.10.540107; this version posted May 10, 2023. The copyright holder for this preprint (which was not certified by peer review) is the author/funder. All rights reserved. No reuse allowed without permission.

MATERIALS AND METHODS

Bacterial strains and growth conditions

Strains used in this study are listed below. Strains were streaked from -80°C freezer glycerol stocks onto Nutrient Agar (NA) plates containing the relevant antibiotics and/or inducers and grown overnight at 37°C. Starter cultures were prepared from a single colony in S750^{glucose} media and grown with orbital agitation at 175 rpm overnight at 37°C. The next day, overnight cultures were diluted to an OD_{600} of 0.05-0.1 in S750^{glucose} media and grown at 30°C with orbital agitation at 175 rpm with any required inducer until they reached the appropriate OD_{600}. Liquid cultures were grown in flasks with at least a 1:20 culture to flask volume ratio. Overnight cultures were grown in either 2 ml or 5 ml volumes, where day cultures were always grown in 5 ml volumes.

Microscopy was performed at 30°C. When necessary, antibiotics and inducers were used at the following final concentrations: chloramphenicol 5 µg/ml, spectinomycin 60 µg/ml, erythromycin 1 µg/ml, lincomycin 10 µg/ml, kanamycin 5 µg/ml, xylose 0.08% and IPTG 20 µM. S750 media contains 1 X S750 salts, 1 X Metal mix, 10 mM L-Glutamate (Sigma) and 1 % Carbon source (Glucose or Maltose (VWR)). Metal mix was prepared as a 100 X stock comprising of 2 mM Hydrochloric Acid (HCl) (Honeywell), 190 mM Magnesium Chloride Hexahydrate (Sigma), 65.9 mM Calcium Chloride Dihydrate (Sigma, 4.84 mM Manganese Chloride Tetrahydrate (Fisher), 0.106 mM Zinc Chloride (Sigma), 0.196 mM Thiamine Chloride (Sigma) and 0.470 mM Iron (III) Chloride Hexahydrate (VWR). S750 salts were prepared as a 10 X stock containing 500 mM MOPS (Sigma), 100 mM Ammonium Sulphate (Sigma), Potassium Phosphate Monobasic (VWR) with pH adjusted to 7.0 with Potassium Hydroxide (VWR).

We found that the following considerations were important for reproducible results: (1) S750 must be made up fresh from the relevant stock solutions no more than 1-2 days before the experiments (see S750 preparation protocol in Supplementary Note 2). (2) cells must be cultured in highly aerobic conditions, here in 2-5 ml volumes in 125 ml conical flasks – notable *not* in 16 ml volume test tubes, (3) cells should be given 10 minutes to recover after being immobilized on the agarose pad before acquiring microscopy data. Deviations from these requirements led to decreased elongasome speed or reduced ratio of motile: immobile elongasomes.

Strain construction

All strains are derived from the PY79 strain [20]. All experimental strains were constructed with the *Δhag* mutant to disable flagellar motility and reduce cell chaining for VerCINI experiments [11]. *B. subtilis* was transformed in accordance with standard protocols[21]. Oligonucleotides and strains used in this study are detailed in Supplementary Table 2.

SM01 (*mreB::mreB-HaloTag, Δhag*) was constructed by transforming bYS40 (Hussain et al. 2018) with gDNA containing *hag::erm* from the *Bacillus* knockout erythromycin (BKE) library (Koo et al. 2017), selecting for transformants on erythromycin and lincomycin. The strain was confirmed by PCR amplification of the *hag* region using oSM01 and oSM02.

SM28 (*mreB::mreB-HaloTag, rodA:-Pspac-rodA, Δhag*) was produced by transforming SM01 with gDNA from YK2245 (Emami et al. 2017). Transformants were selected on 100 µM IPTG and kanamycin. The strain was confirmed by simplification of the *rodA* region using oSM15 and oSM43. In addition, the strain was streaked on NA plates in the presence and absence of 100 µM IPTG and was found to be IPTG dependent.

SM22 (*mreB::mreB-HaloTag, Δhag, ΔpbpA*) was constructed by transforming SM01 with gDNA containing *pbpA::kan* from the *Bacillus* knockout kanamycin (BKK) library (Koo et al. 2017), selecting

bioRxiv preprint doi: https://doi.org/10.1101/2023.05.10.540107; this version posted May 10, 2023. The copyright holder for this preprint (which was not certified by peer review) is the author/funder. All rights reserved. No reuse allowed without permission.

for transformants on kanamycin. The strain was confirmed by PCR amplification of the *pbpA* region using oSM19 and oSM20.

SM23 (*mreB::mreB-HaloTag, Δhag, ΔpbpH*) was constructed by transforming SM01 with gDNA containing *pbpH::kan* from the *Bacillus* knockout kanamycin (BKK) library (Koo et al. 2017), selecting for transformants on kanamycin. The strain was confirmed by PCR amplification of the *pbpH* region using oSM27 and oSM28.

SM41 (*mreB::mreB-HaloTag, Δhag, ΔmltG*) was constructed by transforming SM01 with gDNA containing *mltG::kan* from the *Bacillus* knockout kanamycin (BKK) library (Koo et al. 2017), selecting for transformants on kanamycin. The strain was confirmed by PCR amplification of the *mltG* region using oSM78 and oSM79.

All used strains are available on request to the authors.

Growth curves

B. subtilis PY79 and derivative strains were grown overnight at 37°C in $S750^{glucose}$ containing relevant inducers. Overnight cells were diluted to an OD_{600} of 0.05 in $S750^{glucose}$, in a 96-well microtiter plate to a final volume of 200 µl. Growth was monitored for 12 hours using a SPECTROstar Nano plate reader (BMG Labtech) at 30°C.

Cell morphology analysis

Cells were prepared for imaging in $S750^{glucose}$ at 30˚C. Once the cultures had reached OD_{600} 0.6 ± 0.1, Nile Red was added to 200 µl of cells to a working concentration of 1 µg/ml, and incubated at growth temperatures for 10 mins, prepared on agarose microscope slides as described below and cell morphology images recorded using the microscope described below. To measure cell width, a straight-line ROI was drawn over the short axis of the cell in FIJI and an intensity profile plotted. The intensity plots were exported to MATLAB where the centre of each peak and the distance between them were determined by fitting to a tilted circle model [11]. To measure cell length, a straight-line ROI was drawn from the pole to pole, or pole to septum and the length measured in FIJI.

Microscopy

VerCINI on custom single molecule microscopes. Two very similar custom single molecule microscopes were used for experiments. Cells were illuminated with a 561 nm laser (Obis). A 100x TIRF objective (Nikon CFI Apochromat TIRF 100XC Oil) was used. A 200 mm tube lens (Thorlabs TTL200) and Prime BSI sCMOS camera (Teledyne Photometrics) were used for imaging, giving effective image pixel size of 65 nm/pixel. Imaging was done with a custom-built ring-TIRF module operated in ring-HiLO[22] using a pair of galvanometer mirrors (Thorlabs) spinning at 200 Hz. 8 minute time lapses were obtained with 500ms exposure at a power density of 16.9 W/cm^2 at a strobe interval of 6s unless otherwise stated. Power density was calculated based on 2.5 mW illumination power measured at the sample, over an illumination area of approximately 14,800 μm^2.

Structured Illumination Microscopy on a Nikon N-SIM. Cells were illuminated a 561 nm laser (CVI Melles-Griot). A 100x TIRF objective (Nikon CFI Apochromat TIRF 100XC Oil) was used for imaging and an Andor iXon DU897 EMCCD camera was used, with a 2.5x magnifier (Nikon) and standard Nikon tube lens, giving an effective image pixel size of 64 nm/pixel. Cells were illuminated in TIRF-SIM mode, using a 2D-striped pattern. Each SIM image was formed from 9 raw images corresponds to 3 stripe angles and 3 stripe phases. SIM reconstruction was performed using proprietary Nikon software which implements the Gustaffson SIM reconstruction algorithm [23]. Reconstruction was carried out in NIS

bioRxiv preprint doi: https://doi.org/10.1101/2023.05.10.540107; this version posted May 10, 2023. The copyright holder for this preprint (which was not certified by peer review) is the author/funder. All rights reserved. No reuse allowed without permission.

elements using default settings; Illumination modulation contrast was set to 1.00, high resolution noise suppression was set to 1.00 and out of focus blur suppression was set to 0.05.

All microscopy was performed on microscopes equipped with incubators to maintain sample and microscope temperature at 30˚C.

Single Molecule HaloTag labelling with JF-549

At OD_{600} of 0.6 ± 0.1, 500 µl cells were incubated for 15 minutes with JF-549 [12] dissolved in dimethyl sulfoxide (DMSO) to a final concentration of 25 pM at 30˚C with shaking at 175 rpm. Stocks were prepared at concentrations to ensure a working DMSO concentration of <1%. Cells were then washed twice in 500 µl pre-warmed media.

Sample preparation for VerCINI microscopy

Agarose microholes were formed by pouring molten 6% agarose dissolved in media (typically $S750^{glucose}$ unless otherwise stated) onto a silicon micropillar array as described previously [11]. Patterned agarose was transferred into a Geneframe (Thermo Scientific) mounted on a glass slide, and excess agarose was cut away to ensure sufficient oxygen.

Cultures were concentrated 50-fold and 10 µl was applied to the pad, before centrifugation at 3,220 RCF for 4 minutes (Eppendorf 5810 centrifuge with MTP/Flex buckets). Pads were then washed with pre warmed media before application of the cover slip (VWR 22 × 22 mm2 Thickness no. 1.5).

VerCINI data analysis

Pre-processing

Videos were denoised using the ImageJ plugin PureDenoise [24], which is based on wavelet decomposition. For the largest image dataset- 0.5 s frame interval measurements in Figure 1e – a GPU-accelerated version of PureDenoise was developed and used (http://www.GitHub.com/ZikaiSun/PureGpu). This version also corrects a memory leak bug for large images in the original PureDenoise ImageJ plugin. Performance characterization of PureDenoiseGPU is shown in Supplementary Tables 5-6.

Denoised videos were registered using the ImageJ plugin StackReg [25]. Cropped region of interest (ROI) movies containing single in-focus cells were manually selected and exported for analysis using the publically available scripts (https://github.com/HoldenLab/Ring_Analysis_IJ)

Images were background subtracted and kymographs extracted using a custom fitting model of diffuse out-of-focus cytoplasmic background plus localized protein signal as previously described [11].

Kymograph analysis of MreB single molecule dynamics.

In ImageJ, a segmented line ROI was manually traced over each track, with segments indicating manually identified processive or paused subtracks. For each kymograph, an ROI set was saved. Using a custom FIJI plugin, 'Export_XY_Coords.ijm', the coordinates of each point in each track were exported to a '.csv' file. The coordinates of each track were analysed using custom python script 'Track data analysis-Full_.ipynb', to determine MreB filament binding dynamics including bound lifetime, processivity. The required Analysis code is available: https://github.com/HoldenLab/Kymograph-spt-analysis

Stroboscopic analysis of photobleaching and MreB binding lifetime.

We analysed MreB subunit unbinding lifetime and JF549 photobleaching lifetime using the stroboscopic illumination method of Gebhardt and coworkers [14]. Using a fixed illumination and

bioRxiv preprint doi: https://doi.org/10.1101/2023.05.10.540107; this version posted May 10, 2023. The copyright holder for this preprint (which was not certified by peer review) is the author/funder. All rights reserved. No reuse allowed without permission.

exposure time of 500 ms, we systematically increased the total time interval between frames, the strobe interval, and measured the apparent lifetime of labelled MreB molecules for each condition (Fig. 1d-e). We calculated the median lifetime of each dataset, with 95 % CIs calculated by bootstrapping. We then fit the median lifetime data to the equation,

$$\tau_{obs} = \Delta t \Big/ \left(\frac{t_{exp}}{\tau_{bl}} + \frac{\Delta t}{\tau_{off}} \right),$$

where Δt is the strobe interval (the x-axis), τ_{obs} is the apparent lifetime, t_{exp} is the fixed 500 ms exposure time, τ_{bl} is the JF549 photobleaching lifetime and τ_{off} is the MreB subunit unbinding lifetime. By fitting the data to the median apparent lifetimes, we obtained estimates of median τ_{bl} and τ_{off}, rather than mean, consistent with the rest of the statistics in the manuscript. We obtained 95 % CI estimates for τ_{bl} and τ_{off} by bootstrap resampling of the inputs into the stroboscopic fitting equation.

Switching rate analysis.

We calculated single molecule switching rates (reversal, pausing, unbinding, initiation) by counting the number of each transition type from immobile or processive states, and dividing by the total duration of all immobile or processive states observed in the dataset [26]. 95 % confidence intervals on the switching rate were calculated by bootstrap sampling of individual tracks from the dataset.

Statistics

Experiments were conducted in biological duplicate because variation between clonal bacterial samples was low, as estimated based on small range measured in replicate medians, unless otherwise indicated.

Averages reported were median values unless otherwise indicated. Medians of biological replicates are shown on figures as white-filled circles. 95% confidence interval of the median, or of the difference of medians, was estimated by bootstrapping. Interquartile range was indicated by IQR. Thick error bar lines in violin plots indicate interquartile range, thin lines indicate adjacent vales. Because variability between single molecules was far greater than the sample-to-sample variation, estimates of uncertainty (95% CIs, IQRs, etc.) were based on the single molecule datapoints. Sample size, indicating number of tracks/ track segments, technical and biological replicates, as appropriate, is presented for each dataset in Supplementary Table 1. Effect size estimates were calculated based on difference of medians, using either DABEST (Data Analysis with Bootstrap Coupled Estimation [27]) or custom bootstrapping scripts. All effect sizes are listed in Supplementary Table 7.

For estimates of the percentage of the population in a specific state (eg percentage of motile tracks), uncertainty is reported to the full data range (*Range)* of all biological replicates.

CODE AVAILABILITY

Open source software for image analysis of VerCINI data was previously described and is available on the Holden Lab GitHub page: https://github.com/HoldenLab/VerciniAnalysisJ, https://github.com/HoldenLab/ring-fitting2,
Open source software for kymograph analysis available on the Holden Lab GitHub page: https://github.com/HoldenLab/Kymograph-spt-analysis.git
Open source PureDenoise-GPU denoising software is available on GitHub: http://www.GitHub.com/ZikaiSun/PureGpu.
Open source software for the tug-of-war simulations: https://github.com/HoldenLab/lipowskiModel

bioRxiv preprint doi: https://doi.org/10.1101/2023.05.10.540107; this version posted May 10, 2023. The copyright holder for this preprint (which was not certified by peer review) is the author/funder. All rights reserved. No reuse allowed without permission.

REFERENCES

[1] A. Vigouroux, B. Cordier, A. Aristov, L. Alvarez, G. Özbaykal, T. Chaze, E.R. Oldewurtel, M. Matondo, F. Cava, D. Bikard, S. van Teeffelen, Class-A penicillin binding proteins do not contribute to cell shape but repair cell-wall defects, ELife. 9 (2020) e51998. https://doi.org/10.7554/eLife.51998.

[2] M.F. Dion, M. Kapoor, Y. Sun, S. Wilson, J. Ryan, A. Vigouroux, S. van Teeffelen, R. Oldenbourg, E.C. Garner, Bacillus subtilis cell diameter is determined by the opposing actions of two distinct cell wall synthetic systems, Nat. Microbiol. 4 (2019) 1294–1305. https://doi.org/10.1038/s41564-019-0439-0.

[3] H. Cho, C.N. Wivagg, M. Kapoor, Z. Barry, P.D.A. Rohs, H. Suh, J.A. Marto, E.C. Garner, T.G. Bernhardt, Bacterial cell wall biogenesis is mediated by SEDS and PBP polymerase families functioning semi-autonomously, Nat. Microbiol. 1 (2016) 16172. https://doi.org/10.1038/nmicrobiol.2016.172.

[4] F. van den Ent, T. Izoré, T.A. Bharat, C.M. Johnson, J. Löwe, Bacterial actin MreB forms antiparallel double filaments, ELife. 3 (2014). https://doi.org/10.7554/eLife.02634.

[5] S. Hussain, C.N. Wivagg, P. Szwedziak, F. Wong, K. Schaefer, T. Izoré, L.D. Renner, M.J. Holmes, Y. Sun, A.W. Bisson-Filho, S. Walker, A. Amir, J. Löwe, E.C. Garner, MreB filaments align along greatest principal membrane curvature to orient cell wall synthesis, ELife. 7 (2018) e32471. https://doi.org/10.7554/eLife.32471.

[6] S. Dersch, C. Reimold, J. Stoll, H. Breddermann, T. Heimerl, H.J. Defeu Soufo, P.L. Graumann, Polymerization of Bacillus subtilis MreB on a lipid membrane reveals lateral co-polymerization of MreB paralogs and strong effects of cations on filament formation, BMC Mol. Cell Biol. 21 (2020) 76. https://doi.org/10.1186/s12860-020-00319-5.

[7] J. Domínguez-Escobar, A. Chastanet, A.H. Crevenna, V. Fromion, R. Wedlich-Söldner, R. Carballido-López, Processive Movement of MreB-Associated Cell Wall Biosynthetic Complexes in Bacteria, Science. 333 (2011) 225–228. https://doi.org/10.1126/science.1203466.

[8] E.C. Garner, R. Bernard, W. Wang, X. Zhuang, D.Z. Rudner, T. Mitchison, Coupled, Circumferential Motions of the Cell Wall Synthesis Machinery and MreB Filaments in B. subtilis, Science. 333 (2011) 222–225. https://doi.org/10.1126/science.1203285.

[9] S. van Teeffelen, S. Wang, L. Furchtgott, K.C. Huang, N.S. Wingreen, J.W. Shaevitz, Z. Gitai, The bacterial actin MreB rotates, and rotation depends on cell-wall assembly, Proc. Natl. Acad. Sci. 108 (2011) 15822–15827. https://doi.org/10.1073/pnas.1108999108.

[10] S. Dersch, J. Mehl, L. Stuckenschneider, B. Mayer, J. Roth, A. Rohrbach, P.L. Graumann, Super-Resolution Microscopy and Single-Molecule Tracking Reveal Distinct Adaptive Dynamics of MreB and of Cell Wall-Synthesis Enzymes, Front. Microbiol. 11 (2020) 1946. https://doi.org/10.3389/fmicb.2020.01946.

[11] K.D. Whitley, S. Middlemiss, C. Jukes, C. Dekker, S. Holden, High-resolution imaging of bacterial spatial organization with vertical cell imaging by nanostructured immobilization (VerCINI), Nat. Protoc. 17 (2022) 847–869. https://doi.org/10.1038/s41596-021-00668-1.

[12] J.B. Grimm, B.P. English, J. Chen, J.P. Slaughter, Z. Zhang, A. Revyakin, R. Patel, J.J. Macklin, D. Normanno, R.H. Singer, T. Lionnet, L.D. Lavis, A general method to improve fluorophores for live-cell and single-molecule microscopy, Nat. Methods. 12 (2015) 244–250. https://doi.org/10.1038/nmeth.3256.

[13] C. Billaudeau, Z. Yao, C. Cornilleau, R. Carballido-López, A. Chastanet, MreB Forms Subdiffraction Nanofilaments during Active Growth in Bacillus subtilis, MBio. 10 (2019). https://doi.org/10.1128/mBio.01879-18.

[14] J.C.M. Gebhardt, D.M. Suter, R. Roy, Z.W. Zhao, A.R. Chapman, S. Basu, T. Maniatis, X.S. Xie, Single-molecule imaging of transcription factor binding to DNA in live mammalian cells, Nat. Methods. 10 (2013) 421–426. https://doi.org/10.1038/nmeth.2411.

bioRxiv preprint doi: https://doi.org/10.1101/2023.05.10.540107; this version posted May 10, 2023. The copyright holder for this preprint (which was not certified by peer review) is the author/funder. All rights reserved. No reuse allowed without permission.

[15] C. Billaudeau, A. Chastanet, Z. Yao, C. Cornilleau, N. Mirouze, V. Fromion, R. Carballido-López, Contrasting mechanisms of growth in two model rod-shaped bacteria, Nat. Commun. 8 (2017) 15370. https://doi.org/10.1038/ncomms15370.

[16] R. Yunck, H. Cho, T.G. Bernhardt, Identification of MltG as a potential terminase for peptidoglycan polymerization in bacteria, Mol. Microbiol. 99 (2016) 700–718. https://doi.org/10.1111/mmi.13258.

[17] M.A. Welte, Bidirectional Transport along Microtubules, Curr. Biol. 14 (2004) R525–R537. https://doi.org/10.1016/j.cub.2004.06.045.

[18] P. v. Olshausen, H.J. Defeu Soufo, K. Wicker, R. Heintzmann, P.L. Graumann, A. Rohrbach, Superresolution Imaging of Dynamic MreB Filaments in B. subtilis—A Multiple-Motor-Driven Transport?, Biophys. J. 105 (2013) 1171–1181. https://doi.org/10.1016/j.bpj.2013.07.038.

[19] M.J.I. Müller, S. Klumpp, R. Lipowsky, Tug-of-war as a cooperative mechanism for bidirectional cargo transport by molecular motors, Proc. Natl. Acad. Sci. 105 (2008) 4609–4614. https://doi.org/10.1073/pnas.0706825105.

[20] P.J. Youngman, J.B. Perkins, R. Losick, Genetic transposition and insertional mutagenesis in Bacillus subtilis with Streptococcus faecalis transposon Tn917., Proc. Natl. Acad. Sci. U. S. A. 80 (1983) 2305–2309.

[21] C.R. Harwood, S.M. Cutting, Molecular biological methods for Bacillus, Wiley, 1990. https://scholar.google.com/scholar_lookup?title=Molecular+biological+methods+for+Bacillus&author=Harwood%2C+Colin+R.&publication_year=1990 (accessed July 19, 2022).

[22] K.L. Ellefsen, J.L. Dynes, I. Parker, Spinning-Spot Shadowless TIRF Microscopy, PLOS ONE. 10 (2015) e0136055. https://doi.org/10.1371/journal.pone.0136055.

[23] M.G.L. Gustafsson, Surpassing the lateral resolution limit by a factor of two using structured illumination microscopy. SHORT COMMUNICATION, J. Microsc. 198 (2000) 82–87. https://doi.org/10.1046/j.1365-2818.2000.00710.x.

[24] F. Luisier, C. Vonesch, T. Blu, M. Unser, Fast interscale wavelet denoising of Poisson-corrupted images, Signal Process. 90 (2010) 415–427. https://doi.org/10.1016/j.sigpro.2009.07.009.

[25] P. Thevenaz, U.E. Ruttimann, M. Unser, A pyramid approach to subpixel registration based on intensity, IEEE Trans. Image Process. 7 (1998) 27–41. https://doi.org/10.1109/83.650848.

[26] G. Özbaykal, E. Wollrab, F. Simon, A. Vigouroux, B. Cordier, A. Aristov, T. Chaze, M. Matondo, S. van Teeffelen, The transpeptidase PBP2 governs initial localization and activity of the major cell-wall synthesis machinery in E. coli, ELife. 9 (2020) e50629. https://doi.org/10.7554/eLife.50629.

[27] J. Ho, T. Tumkaya, S. Aryal, H. Choi, A. Claridge-Chang, Moving beyond P values: data analysis with estimation graphics, Nat. Methods. 16 (2019) 565–566. https://doi.org/10.1038/s41592-019-0470-3.